ACS NANO

www.acsnano.org

ARTICLE

# Block Copolymer Self-Assembly-Directed and Transient Laser Heating-Enabled Nanostructures toward Phononic and Photonic Quantum Materials

Fei Yu,[⊥] Qi Zhang,[⊥] R. Paxton Thedford, Andrej Singer, Detlef-M. Smilgies, Michael O. Thompson, and Ulrich B. Wiesner*

Cite This: *ACS Nano* 2020, 14, 11273–11282

Read Online

ACCESS | Metrics & More | Article Recommendations | Supporting Information

**ABSTRACT:** Three-dimensional (3D) periodic ordering of silicon (Si), an inorganic semiconductor, on the mesoscale was achieved by combining block copolymer (BCP) self-assembly (SA) based mesoporous alternating gyroidal network formation with non-equilibrium transient laser heating. 3D continuous and periodically ordered alternating gyroidal mesoporous carbon thin-film networks were prepared from spin coating, SA under solvent vapor annealing (SVA), and thermal processing of mixtures of a triblock terpolymer with resorcinol resols. The resulting mesoporous thin films, acting as structure-directing templates, were backfilled with amorphous silicon (a-Si). Nanosecond excimer laser heating led to transient Si melts conformally filling the template pores and subsequent Si crystallization. The ordered mesostructure of the organic polymer-derived templates was kept intact, despite being thermally unstable at the high temperatures around the Si melting point (MP), leading to high pattern transfer fidelity. As evidenced by a combination of grazing incidence small-angle X-ray scattering (GISAXS) and scanning electron microscopy (SEM), after template removal, the crystalline Si (c-Si) inherited the inverse network topology of the 3D mesoporous thin-film templates, but with reduced *F*222 space group symmetry ($D_2$ point group symmetry) from compression of the cubic alternating gyroid lattice. Structures with this reduced symmetry have been proposed as photonic and phononic materials exhibiting topologically protected Weyl points, adding to the emerging field of BCP SA-directed quantum materials promising advanced physics and materials properties.

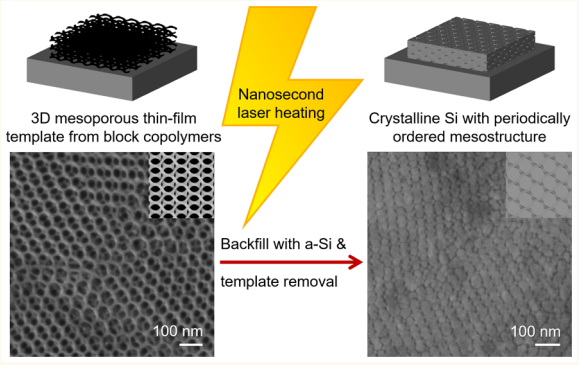


**KEYWORDS:** *block copolymer self-assembly, 3D network template, transient laser heating, nonequilibrium processing, quantum materials*

The adoption of molds to produce objects with well-defined structures has been an integral part of the development of human civilization. Today, injection molding of polymers is ubiquitous, e.g., in auto parts manufacturing and the packaging industry. With the advent of nanoscience and nanotechnology, our ability to make even more intricate structures has been advanced by the design of "nanomolds", with lithography being the most widely used technology in this regard.[1] Such top-down approaches usually produce two-dimensional (2D) patterns in a single fabrication cycle. More complex molds (or templates), particularly those with periodic three-dimensional (3D) connectivity, necessitate multistep fabrication processes. On the other hand, feature sizes of 3D templates from one-step bottom-up strategies such as colloidal self-assembly (SA) are typically restricted to over 100 nm.[2,3]

Block copolymer (BCP) SA offers an alternative pathway toward realizing 3D nanomolds by forming structures such as hexagonal or 3D cocontinuous gyroidal mesophases with a mesoscale periodicity (tens of nanometers).[4−6] By adding nanoparticles or other organic or inorganic precursors that

Received: April 14, 2020
Accepted: August 11, 2020
Published: August 11, 2020






https://dx.doi.org/10.1021/acsnano.0c03150
*ACS Nano* 2020, 14, 11273–11282

preferentially swell specific blocks and are small enough,[7] the resulting hybrids of BCPs and nanoparticles/additives undergo microphase segregation together (or coassemble) to form a variety of BCP SA-directed mesophases, including 3D cocontinuous network morphologies.[8−10] Mesoporous nanomolds with feature sizes or periodicities typically below 100 nm are finally obtained after selective degradation of block domains in the case of all-organic hybrid materials or high temperature processing in the case of inorganic additives.[11−14] There have previously been attempts to incorporate BCPs in one-step nanofabrication approaches to 3D mesostructures. The resulting nanomolds are not comprised of intrinsically 3D interconnecting networks, however, but rather exhibit stackings of mesostructures of lower dimensions[15,16] and require additional complex fabrication steps such as chemical or topographic patterning of the substrates.[15,17]

Bulk mesoporous structures with either double or alternating gyroidal morphologies of polymer resin-based carbons have been demonstrated from selectively mixing phenol or resorcinol resols with the poly(ethylene oxide) (PEO) blocks of the triblock terpolymer (TTP) poly(isoprene-*b*-styrene-*b*-ethylene oxide) (PI-*b*-PS-*b*-PEO, referred to as ISO hereafter), followed by cross-linking and carbonization.[18,19] The resistance of the resulting amorphous carbons to electrochemical corrosion and silica etching agents, as well as their removal by simple oxidation,[14] establishes them as a robust and convenient mesoporous scaffold for templating of other materials.[20,21]

Although mesoporous materials derived from BCP SA allow for backfilling with other materials, this is challenging to achieve in bulk monoliths with thicknesses beyond tens of micrometers. This is true even for periodically ordered cocontinuous network gyroidal structures, due to limited diffusivity in the tortuous passageways deep inside.[22,23] Thin films below approximately 1 $\mu$m thickness are therefore the preferred sample geometry. While it is possible to cut bulk materials into such thin pieces using a microtome, the constraint on the area of the thin sections (limited by the original bulk cross-section) renders this approach unscalable and time-consuming. Furthermore, unless macroscopic single crystalline BCP samples are used, the orientation of the mesostructure with respect to the substrate is often random and difficult to control.[24,25]

We have recently shown that large-area, periodically ordered resin/carbon thin films with 3D double or alternating gyroid network structures and well-defined orientations can be prepared via solvent vapor annealing (SVA) and subsequent pyrolysis of ISO−resols composite films directly spin-coated on unpatterned substrates.[26] With their large and accessible pores, a wide range of materials such as metals and semiconductors can be backfilled into the void network, which intertwines with the gyroidal carbon network, by well-established thin-film deposition techniques. Furthermore, we developed a method by which these thin films can be transferred to any arbitrary substrate.[26] These strategies can potentially usher in advanced structural designs based on BCP SA for inorganic materials, which alone cannot access desirable periodically ordered 3D continuous structures on the mesoscale.[27,28]

A prerequisite of utilizing molds is their structural stability under the processing conditions of the templated materials. In air, carbon resin templates derived from BCP SA cannot withstand high temperatures commonly encountered in inorganic materials processing. If the backfilled inorganic materials are amorphous, effective annealing processes in order to obtain fully crystalline phases conformally filling the carbon templates *via*, *e.g.*, furnace annealing or rapid thermal annealing typically leads to template decomposition or collapse during long (at least seconds or longer) annealing times at temperatures approaching the melting point (MP) of many inorganics (often easily exceeding 1000 °C).

While the equilibrium thermodynamics governing BCP SA during SVA offers pathways to periodically ordered mesostructures for the templates, a key to exploring such unconventional nanomolds for inorganic materials fabrication may lie in nonequilibrium processing. The decomposition of organic materials is enormously suppressed as the heating duration is scaled down from seconds to micro- and nanoseconds.[29,30] As energy-intensive tools, lasers are able to deliver the required amounts of energy for materials transformations within such extremely short time frames.[24,30] If the materials systems are pushed far away from equilibrium, so that the transformations are faster than the oxidation kinetics of the organic (e.g., resin/carbon network) structures, organic material-based templates can be maintained far beyond their regular temperature stability limits. Previous efforts at employing such transient laser annealing techniques in air yielded epitaxially grown single-crystal inorganic materials like Si (a semiconductor) or NiSi (a metal) confined in mesoporous metal oxide templates derived from BCP SA.[31] In these experiments, the thin-film oxides were kinetically trapped in disordered mesostructures that could not be further annealed after spin-coating as a result of the irreversible condensation of the metal oxide precursors during the sol−gel process. This limitation could be overcome by moving to BCP SA-directed resols-derived mesostructures, which allow SVA before pore formation.[24,25] However, these studies employed cryo-microtomed thin film sections of bulk samples deposited on single crystal substrates (*vide supra*) and did not include detailed crystallographic analysis of the resulting structures.

Here, we report the application of transient laser annealing on Si backfilled into large-area, thin-film carbon templates, with ordered 3D alternating gyroid network structures derived from BCP SA and SVA. This combines previous work on preparing spin-coated BCP SA-directed resin/carbon thin film templates with periodically ordered 3D mesostructures through SVA in a scalable and facile manner with nonequilibrium nanosecond laser heating of such templates backfilled with amorphous Si (a-Si). To the best of our knowledge, this combination has not been achieved before, but is of substantial interest as it enables the translation of periodic BCP SA derived thin film structures into 3D periodic inorganic materials, including but not limited to semiconductors, using the standard processing methodology of the semiconductor industry. Si was chosen as the model backfilling material not only for its technological significance as a semiconducting inorganic material but also for its high processing temperature. This will help with demonstration and understanding of the effects and limitations of nonequilibrium processing on the formation of mesostructured materials confined and crystallized in templates with 3D network topology. Crucially, detailed examination of the symmetry of the resulting ordered mesostructures as a function of thin film processing, as revealed by a combination of grazing incidence small-angle X-ray scattering (GISAXS) and scanning electron microscopy (SEM), suggests that the final composite and templated Si mesostructures are consistent with the space


https://dx.doi.org/10.1021/acsnano.0c03150
ACS Nano 2020, 14, 11273−11282

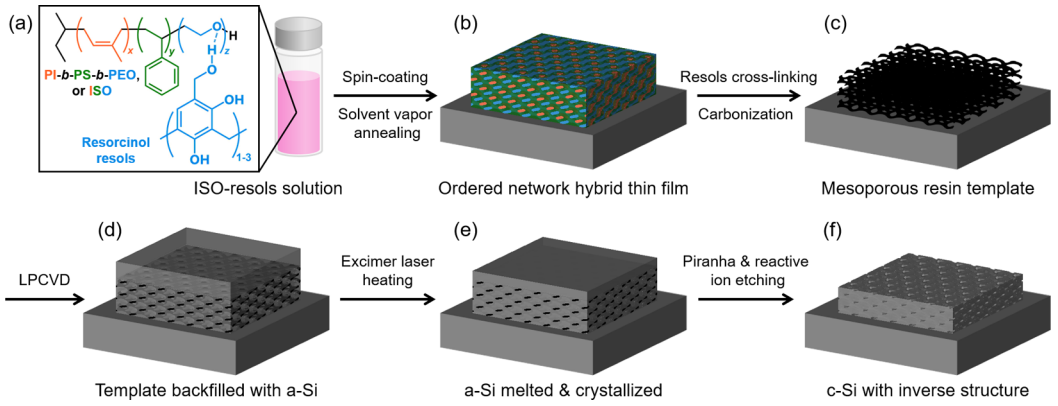


**Figure 1. Schematic of the fabrication process. (a) ISO and resorcinol resols hybrid solution, with the chemical structures of ISO and resols shown in different colors corresponding to microphase-segregated domains after self-assembly. (b) ISO–resols hybrid thin film on a silicon substrate after spin-coating and solvent vapor annealing (SVA). (c) Mesoporous resin/carbon thin-film network after cross-linking and carbonizing ISO–resols hybrids in nitrogen at temperatures between 450 and 600 °C. (d) Amorphous silicon (a-Si) backfilled into the template through low pressure chemical vapor deposition (LPCVD), with an overlayer of a-Si on top. (e) a-Si is melted by transient excimer laser heating and crystallized in the template. (f) Mesostructured crystalline silicon (c-Si) with the inverse structure of the resin/carbon template after template removal by reactive ion etching (RIE) and piranha etching.**

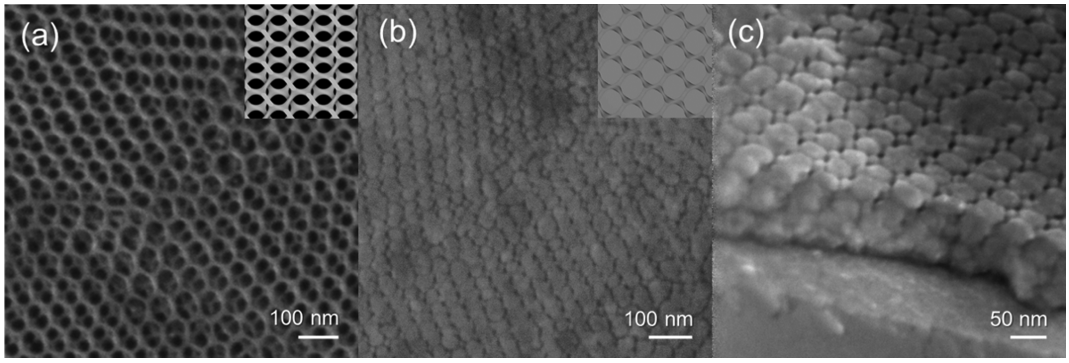


**Figure 2. Plan-view scanning electron microscopy (SEM) images of (a) a mesoporous carbon network thin film after cross-linking and carbonizing ISO–resols hybrid in nitrogen and (b) final mesostructured crystalline silicon (c-Si) with the inverse structure of the template after its removal. A 45° oblique view of the final mesostructured c-Si is shown in (c). Insets in (a) and (b) show expected structures along ⟨110⟩ from level set calculations (see also Figure S1) consistent with observations.**

group *F*222. As we have shown earlier in a theoretical study,[32] this reduced symmetry, equivalent to $D_2$ point group symmetry resulting from deformation of the cubic alternating gyroid lattice upon processing, could enable the construction of BCP SA-based photonic and phononic quantum metamaterials with topologically protected Weyl points. The study therefore points in the direction of the emerging field of BCP SA-based quantum materials, promising advanced physics and unusual materials properties.[33]

## RESULTS AND DISCUSSIONS

**Template Formation, a-Si Backfilling, and Transient Laser Annealing.** In our work, BCP SA-directed network mesophase formation is the basis for creating 3D periodically ordered mesostructures, which after SVA and thermal processing act as templates (molds) for backfilling with inorganic materials. Transient laser heating-induced melting and conformal backfilling of the mold, followed by template removal, results in the desired inorganic mesostructures. Figure 1 provides a schematic illustration of the processing workflow followed in this study, while experimental details for each step are described in the Methods section. The TTP ISO (Figure 1a) has been thoroughly characterized,[34] and its phase diagram shows several network structures that are stable over a wider range of compositions (~10–14%) as compared to diblock copolymers (~2–4%).[35,36] Nanoparticles or other organic or inorganic material precursors can selectively swell only one of the BCP blocks, thereby giving rise to self-assembled mesostructures of various other materials that lack SA abilities. This BCP-nanoparticle/additive coassembly strategy confers materials diversity and advanced functionalities to otherwise purely organic soft BCP materials and has been pursued and realized in a number of systems, ranging from binary,[14] ternary,[37] and quaternary[38] oxides or nitrides, through metals,[39] ceramics,[40] carbides,[41] and carbons,[19] all the way to semiconductors and superconductors.[33]

Upon careful mixing in tetrahydrofuran (THF) to ensure the appropriate block volume ratios, oligomeric carbon precursors, resols, form hydrogen bonds with the PEO block of ISO (Figure 1a) and produce two types of cubic network mesophases after spin coating and SVA in THF (see Methods): the core–shell double gyroid ($G^D$, space group $Ia\bar{3}d$, referred to as $Q^{230}$) and the chiral alternating gyroid ($G^A$, space group $I4_132$, referred to as $Q^{214}$), which on the length scale of a local grain is a chiral structure.[19] After the resols are cross-linked at moderate temperatures of around 120 °C in the


https://dx.doi.org/10.1021/acsnano.0c03150
ACS Nano 2020, 14, 11273–11282

presence of the ISO, heat treatment in the inert atmosphere such as nitrogen at higher temperatures (around 450 °C) will decompose the ISO and further cross-link and carbonize the resols, introducing mesoporosity to the now highly cross-linked but still polymer−organic gyroids.[24,25] Further heat treatments in the inert atmosphere at temperatures of 600 °C or beyond will finally lead to inorganic turbostratic glassy carbons.[19] Since in a gyroid each block domain constitutes a 3D continuous network, the mesopores therefore form a 3D continuous void network, allowing uninterrupted passageways throughout an entire macroscopic monolith. Such ordered mesoporous networks are promising candidates for use as nanomolds to direct 3D continuous structures of backfilled materials with a resolution that is as yet beyond what can be accomplished today by other means such as 3D printing.[42]

We first synthesized an ISO with 30.6 vol % PI, 60.8 vol % PS, and 8.6 vol % PEO that would structure-direct resorcinol resols to generate $G^A$ hybrids (Figure 1a,b). The $G^A$ morphology was preferred over the $G^D$ structures due to the smaller volume fraction of the PEO + resols domain, leading to larger, more accessible mesopores after thermal processing. As alluded to previously, we worked with spin-coated thin films rather than bulk materials, as the former are better suited for complete backfilling. SVA was performed to improve long-range periodic ordering in the thin-film structure (Figure 1b), as rapid solvent evaporation during spin-coating typically freezes metastable structures on their way to equilibrium. Plan-view SEM images (Figure 2a) of the mesoporous network after cross-linking and further heat treatment at up to 600 °C (Figure 1c) showed highly regular mesoporosity. The self-assembled thin films were also highly textured, with the {110} planes parallel to the surface. This was corroborated by simulated $G^A$ networks from level set calculations (Figure 2a, inset). The internal network struts gradually faded out of the depth of field of the electron microscope, denoting 3D continuity. The mesopore diameter was around 45 nm, as measured from the area enclosed by the carbon strut loops on the surface. The thermal processing temperature should be high enough to decompose the ISO for creating mesoporosity at a minimum of around 450 °C. While the cross-linked resols could undergo more complete carbonization into graphitic carbons at even higher temperatures, samples were treated at 600 °C to reduce the processing time, while still maintaining structural integrity during the following steps, including low pressure chemical vapor deposition (LPCVD) at 570 °C (Figure 1d, see Methods). During pyrolysis, the film thickness as estimated from SEM images of film cross sections decreased from around 450 nm to around 200 nm (data not shown) as the ISO−resols hybrid was gradually carbonized starting at 600 °C, consistent with earlier observations of such BCP−additive hybrids.[26,43] It should be emphasized that all explored heat treatments took place at temperatures considerably lower than the MP of 1410 °C for crystalline Si (c-Si).

Prior to depositing a-Si into the mesoporous template, the resin/carbon thin-film networks were cleaned by aqueous hydrochloric acid (HCl) and hydrogen peroxide ($H_2O_2$) according to standard wafer cleaning protocols (see Methods).[44] Organic residues and particles remaining after template fabrication in general lab environments were removed for the cleanroom operation in LPCVD furnaces. A hydrofluoric acid (HF) dip was carried out to create a clean oxide-free substrate surface for a-Si deposition (e.g., areas on the Si substrate not covered by the mesoporous template). The 10-min dip of the HF protocol did not lead to delamination of the film from the Si substrate. Although efforts were made to minimize the time between taking the samples out of the HF bath and loading them into the LPCVD furnace, native oxide likely regrew during procedures including rinsing with deionized (DI) water, blow-drying, the sample tray moving into the furnace, and pumping the chamber down. During deposition, a-Si entered the 3D mesoporous void space (Figure 1d). Despite overgrowing the template, the resulting a-Si surface was reminiscent of the carbon template (Figure S2), as the a-Si grew in mounds emanating from the pores. The 50 to 100 nm thick a-Si overlayer on top of the template film encapsulated the underlying template (Figure S3); this overlayer was found to be important for protecting the template during the harsh transient laser annealing conditions against oxidation, structural collapse, and/or photoablation.[45] Higher magnification SEM images of a-Si grown on bare Si wafers (without a template) under the same conditions revealed feature sizes drastically different from the length scale of the gyroidal templates (Figure S4), offering proof that the mesoporous template network was instrumental in shaping the mesostructures of Si.

After a-Si deposition, transient laser heating was accomplished using a 35 ns fwhm, 308 nm wavelength, XeCl excimer laser incident perpendicularly to the thin film surface at a fluence sufficient to melt c-Si as described earlier (Figure 1e).[24,31] Subsequent template removal (Figure 1f) was completed via a combination of dry etch and wet etch methods. $CF_4$ plasma etching removed the Si overlayer, and subsequent $O_2$ plasma etching followed by HF dips exposed the carbon template for oxidative etching in a piranha solution. Figure 2b presents an SEM plan-view image of the resulting mesostructured Si, where channels left behind by the template were imprinted in the laser-annealed Si. The Si mesostructures, which took on the structural inverse of the carbon template, had much smaller pore sizes than the template itself. This is due to the low spatial occupancy (but large pores) of the alternating gyroid network, derived from the minority block of PEO plus resols (24 vol % in the hybrid before pyrolysis). Level set simulations predicted a similar top surface of semiconnected channels running through Si (Figure 2b, inset), further confirming excellent pattern transfer fidelity. The sharp edges in the simulated image come from spatial definition along {110} planes in the calculation setting and likely are blunted during the etching processes. The appearance of {110} planes varied at different vertical positions of the film. The top view displayed in Figure 2b is close to the plane that had the largest areal fraction of the now voided network domains (Figure S1). It best illustrates the 3D interweaving of Si with the carbon template as well as the footprint of the template on the mesostructured Si after template removal. The small spacing between neighboring planes with the same Miller index required stringent control over the multistep etching process, for a slight shift of the final etch front would produce a vastly different surface morphology (Figure S1). Mesoscale ordering could also be confirmed from the 45° oblique view of the edge of a cleaved sample (Figure 2c). On average about 2 to 3 repeating units across the film normal could be observed. It is interesting to note that the resulting mesostructured Si films were thinner than the template after pyrolysis. We attribute this observation to the disruption of the top network structure during a-Si deposition and laser annealing (*vide infra*), as well as the etching process


https://dx.doi.org/10.1021/acsnano.0c03150
ACS Nano 2020, 14, 11273−11282

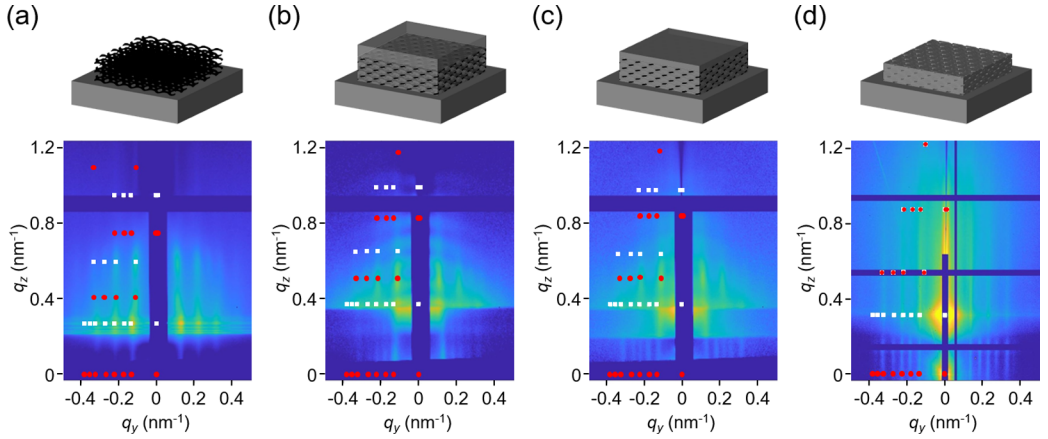


**Figure 3. Grazing incidence small-angle X-ray scattering (GISAXS) patterns at different fabrication stages of mesostructured thin films. (a) Mesoporous carbon thin film after thermal processing; (b) amorphous silicon (a-Si) backfilled into the carbon template; (c) a-Si melted and crystallized in the template after transient laser annealing; and (d) final mesostructured crystalline silicon (c-Si) after template removal. White squares and red dots are the expected peak positions through reflection and transmission channels, respectively, in GISAXS, as calculated by the distorted wave Born approximation theory using the GIXSGUI package (see Methods). Rows of peaks move along the $q_z$ axis as a result of X-rays incident at different angles on samples with different refractive indices. Expected peaks are shown on only the left half of each GISAXS pattern for easier comparison with experimental peak positions on the right half.**

to reveal this specific surface morphology. Oxide formation during transient laser heating is negligible due to the extremely short time scales involved.[46] It is expected, however, that a thin (around 1 nm) oxide layer is present on the surfaces of such large surface area nanostructured Si films, especially when left in the ambient environment. Such oxide layers, with a thickness insignificant relative to the Si strut size around 45 nm, can be etched away, e.g., with HF.

**Thin Film Structure Characterization by X-ray Scattering.** While electron microscopy provides real space and local characterization, X-ray scattering yields structural information averaged over macroscopic volumes of carbon templates and Si mesostructures. GISAXS is well-suited to characterize such thin films with mesoscale ordering by illuminating the sample at incident angles close to the critical angles of total external reflection for the substrate and the supported thin-film materials, thus only probing surface structures. 2D scattering patterns of the thin films at various stages during the fabrication process are shown in Figure 3, fit with expected peak positions calculated according to allowed Bragg diffractions for specific space group symmetries. Earlier analysis had revealed that bulk ISO–resols samples with similar compositions self-assembled into $G^A$ structures belonging to the space group $I4_132$.[19] Although the same cubic $I4_132$ symmetry matched the structure of ISO–resols hybrid thin films in the swollen state during SVA,[26] rapid purging with dry argon to freeze the mesostructure led to dramatic reductions in the film thickness. Consequently, the quenched structure after SVA could only be described, at best, as a compressed $G^A$. Indeed, compressed unit cell parameters ($a$, $b$, $c$, and $\alpha$, $\beta$, $\gamma$) optimized for best fitting of GISAXS patterns deviated substantially from the requirement of $a = b = c$ and $\alpha = \beta = \gamma = 90°$ for a cubic unit cell.[26]

Within the analysis framework of "compressed $G^A$" structures, the carbon thin-film templates were oriented with their {110} planes parallel to the substrate.[26] Although there was a "cubic" $I4_132$ symmetry with altered lattice parameters of $a_1 = b_1 = 47.0$ nm $< c_1 = 71.0$ nm and $\alpha_1 = \beta_1 = 90° < \gamma_1 = 158°$ and this orientation could be invoked to index the 2D GISAXS patterns shown in Figure 3, the congruity between calculated peak positions using the GIXSGUI package and experimental data deteriorated for structures in later stages of the processing flow. Notably, the peaks at $q_y = \pm 0.18$ nm$^{-1}$ in the first-order reflection and transmission channels were missing in the calculated results (Figure 3b–d, Figure S5).

A search for a more accurate description of the actual mesostructural symmetry was therefore warranted, in particular considering that knowledge about the exact symmetry evolution in such thin films may have important consequences in understanding precise structure–property relationships. It is possible to convert a body-centered cubic lattice, to which $I4_132$ belongs, into a face-centered orthorhombic lattice with {010} planes parallel to the substrate (Figure S6) via uniaxial compression along ⟨110⟩ (very notably the direction perpendicular to the substrate). Among the five space groups that have face-centered orthorhombic lattices,[47] $F222$ (space group number 22, hereafter referred to as $O^{22}$, with point group $D_2$ in the Schoenflies notation) is best suited to characterize the symmetry of the structure after film thickness shrinkage. The other four space groups with face-centered orthorhombic lattices can be ruled out as follows. The peaks at $q_y = \pm 0.18$ nm$^{-1}$, unassigned in the cubic lattice (*vide supra*), were found to be (002) and (00$\bar{2}$) peaks in the orthorhombic lattice (see Figure S7 for complete peak indexing with corresponding Miller indices), which do not meet the reflection conditions imposed by the $d$ glide planes in two other space groups with face-centered lattices, $Fdd2$ and $Fddd$ (also referred to in the literature as $O^{70}$). This is further supported by the absence of $d$ glide planes in the original $Q^{214}$ symmetry. The lack of evenness or oddness of the parent (uncompressed) level set equations[48] and the lack of mirror planes in the original $Q^{214}$ symmetry preclude the presence of any mirror planes, which is supported by observations of the network structure simulated by level set calculations (Figure S8). Compression of body-centered cubic lattices of packed micelles yielded face-centered orthorhombic lattices containing mirror planes,[49] since the structure-building blocks were spherical micelles and mirror planes could be drawn before compression (Figure S6). This was not the case with compressed gyroid networks due to their unique connectivity


https://dx.doi.org/10.1021/acsnano.0c03150
ACS Nano 2020, 14, 11273–11282

in 3D space. Therefore, from the remaining space groups with face-centered lattices, *Fmm*2 and *Fmmm*, are also inconsistent with the identified symmetry, leaving space group *F*222 as the only possible solution.

After this symmetry deduction, the optimized set of orthorhombic lattice parameters was found to be $a_2$ = 92.3 nm, $b_2$ = 17.9 nm, $c_2$ = 70.0 nm, and $\alpha_2 = \beta_2 = \gamma_2 = 90°$. These lattice parameters closely matched values from $a_1$, $b_1$, $c_1$ and $\alpha_1$, $\beta_1$, $\gamma_1$ after simple trigonometric transformation from the compressed cubic notation (Figure S6) and exhibited an excellent level of conformity to each measured 2D GISAXS pattern (Figure 3a–d, Figure S9). The (002) and (00$\bar{2}$) peaks emerged as the $4_1$ screw axis in the $I4_132$ space group was broken by dramatic film thickness shrinkage at the end of SVA and during the subsequent heat treatment ($4_1$ screw axes only exist in cubic or tetragonal lattices; see Figure S10 for the GISAXS pattern after SVA but before high temperature heat treatment). We note that similar symmetry breaking from cubic gyroid structures was observed before.[37,50]

This X-ray scattering analysis stands as further testimony to recent identification of structural imperfections in BCP self-assembled mesophases down to the unit cell level by transmission electron microtomography (TEMT)[51] and focused ion beam scanning electron microscopy (FIB-SEM).[52] It is worth noting that our space group assignment does not negate the previous use of "gyroids" to describe these network structures, as the network connectivity/topology was preserved under these deformations (Figure S8). Rather, this work serves as an elucidation of the symmetry details and structural complexities associated with BCP SA structure formation and evolution under nonequilibrium processing conditions.

Each GISAXS pattern at different stages of the fabrication process satisfied the $O^{22}$ space group symmetry with the same set of lattice parameters, confirming the preservation of the highly ordered network structure. However, some structural evolutions could be inferred from subtle changes in the GISAXS patterns. First, the intensities of the (002) and (00$\bar{2}$) peaks (as aforementioned a differentiating feature of $O^{22}$ versus $Q^{214}$) grew stronger after each processing step (see the transmission mode around $q_z$ = 0 in Figure 3). This can be explained as a result of the changing electron density (and hence scattering length) contrast: the contrast in the mesoporous carbon films (Figure 3a, carbon against air) was less than that in Si-filled templates (Figure 3b,c, Si against carbon), which itself was again less than that in mesostructured Si after template removal (Figure 3d, Si against air). Second, we noted that a series of oscillating ripples in the shape of arcs appeared along the $q_z$ direction after a-Si deposition (Figure 3b). From SEM observations the thin films were not perfectly flat (Figure S11), and it is likely that the a-Si overlayer roughness caused the X-rays to spread out as arcs. The appearance of the arcs may also be a result of incomplete pore filling before laser annealing, where void space was less completely filled closer to the substrate. This effectively would translate into another interfacial roughness between filled upper parts and less filled lower parts in the mesoporous template, which also would contribute to the emergence of oscillating ripples. In the experiments, the oscillations became muted after laser heating (Figure 3c), an indication that interface roughness was alleviated when either the molten Si more conformally filled the entire void space, or the surface became flatter, or both. The oscillating ripples disappeared after template removal (Figure 3d), resulting in well-oriented structures, another piece of evidence that they originated from the rough interfaces that disappeared upon processing. Lastly, higher order reflections diminished along $q_z$ beyond the Yoneda band[53] for structures in later stages (Figure 3b–d). As the films became thinner after etching, coherent scattering along the film normal was weaker. This rendered higher-order out-of-plane reflections less pronounced and blurred the in-plane reflections to morph into Bragg rods, which might signify a small loss of 3D periodicity. Nonetheless, laser annealed mesostructured Si in network templates maintained an exceptional $O^{22}$ ordering over a large area after multiple processing steps.

**Transient Si Melts in BCP Templates as Evidenced by Reflectance.** Thermal compatibility of the template and backfilled materials is essential if such nanomolds are to be used to direct the structures of various different classes of materials. Si, an inorganic material, was introduced into the template in the form of a-Si decomposed from $SiH_4$. Polycrystalline Si (poly-Si) annealed from LPCVD-derived a-Si was shown to have superior crystal quality as compared to as-deposited poly-Si.[54] In order to accomplish conformal pore filling and a crystallized state, a-Si had to be melted and solidified at temperatures between the a-Si MP around 1250 °C and the c-Si MP of 1410 °C.[55] By conventional wisdom, a resin or even carbon-based template cannot endure such high temperatures, barring the creation of an oxygen-free environment (our transient laser annealing experiments were performed in air). It has been quantitatively shown that organic polymeric materials can be thermally stabilized by about 400 °C after scaling down the heating duration by 5 orders of magnitude from tens of seconds to microseconds.[29] From our experiments here as well as earlier work, an excimer laser operating with pulse durations as short as ∼40 ns extended the thermal stability of pyrolyzed BCP SA-derived resin mesostructures up to the Si MP.[24,25] Here we employed a similar strategy working with as-made BCP–resols hybrid thin films first cross-linked at 120 °C and then pyrolyzed at 450 or 600 °C before deposition of a-Si at 570 °C through LPCVD at low pressure (see Methods). Although porous nanostructures composed of materials more resistant to high temperatures are in principle available for transient laser heating experiments,[31] the all-organic materials-derived carbon thin-film templates used here (only heat treated up to 600 °C, *i.e.*, below the onset of significant graphitic carbon formation) seem promising for producing the high-quality, long-range mesostructural 3D periodic order as showcased in the resulting c-Si structures. The high degree of ordering is enabled by the application of SVA of the all-organic thin films, an approach well-established for the processing of, in particular, BCP thin films.

Details of the melting and recrystallization of Si during transient laser annealing could be obtained from *in situ* laser reflectance measurements (see Methods). Shortly after the onset of excimer laser irradiation at time $t$ = 0 (Figure 4a), the reflectance recorded by the diode laser (Figure 4b) spiked as the surface a-Si melted into the metallic liquid phase (l-Si), which has substantially higher reflectance than a-Si or c-Si.[56] During the initial melt, thin film interference between the various a-Si, c-Si, and l-Si interfaces caused the reflectance to dip slightly near $t$ = 15 ns (Figure 4b) before reaching the reflectance of an optically thick l-Si film by $t$ = 25 ns. While the initial melt dynamics may include self-propagating explosive crystallization,[55,57] the laser fluence was sufficiently high that


https://dx.doi.org/10.1021/acsnano.0c03150
ACS Nano 2020, 14, 11273–11282

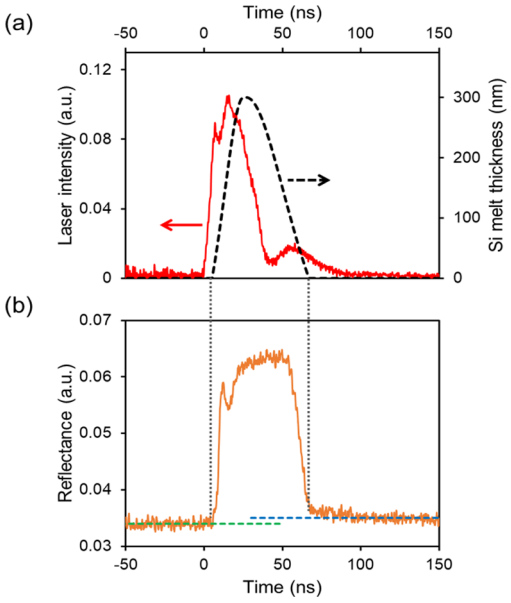


**Figure 4. (a) Excimer laser intensity (red curve) and schematic estimate of the Si melt thickness (black dashed curve) as a function of time. (b) Time-resolved reflectance of Si in the resin/carbon template during transient excimer laser annealing with a fluence of 630 mJ/cm$^2$, as probed by a 650 nm diode laser. The green and blue dashed lines represent the average reflectances before and after melting, respectively.**

the Si throughout the mesoporous template was molten before the final solidification of c-Si began. This ultrafast nanoscale liquid–solid movement was facilitated by the large, open, and 3D interconnected mesopore structure filled originally with a-Si. The Si melt reached its maximum around $t$ = 30 ns near the end of the primary excimer laser intensity peak (Figure 4a), with the reflectance returning to the c-Si value near $t$ = 65 ns as the surface fully crystallized (Figure 4b). When first initiated, the l-Si melt temperature is at the MP of a-Si (1250 °C). However, as the interface just begins to solidify to c-Si at the maximum melt thickness (Figure 4a), the liquid temperature will be the equilibrium melting point of c-Si (1410 °C).[55] Our results therefore show that, despite being under ambient atmosphere (*i.e.*, in the presence of oxygen), the BCP directed carbon networks can withstand temperatures above 1400 °C as a result of the associated ultrashort time scales. We speculate here that the high transient temperatures at the MP of c-Si are responsible, at least in part, for the observed reduction of the film thickness of the final Si nanostructure relative to the original template after pyrolysis (*vide supra*). A boundary between mesostructured Si and the supporting single-crystal Si substrate could still be identified using high-resolution transmission electron microscopy (TEM, Figure S12); this suggests that the 630 mJ/cm$^2$ fluence did not melt sufficiently deep into the substrate to allow for epitaxial growth through the native oxide layer that would have formed after cleaning but prior to the LPCVD deposition (*vide supra*). However, the final reflectance after laser-induced melting was distinct from the reflectance before irradiation (Figure 4b), indicating the formation of c-Si within the carbon template. Subsequent template removal yielded mesoporous c-Si with a void space left behind from the template, all consistent with a 3D network structure. The scattering work of the foregoing section confirmed the generation of mesostructured c-Si directed by the mesoporous network-type nanomolds with *F*222 symmetry over extended areas upward of a millimeter squared.

## CONCLUSIONS

We showed that periodically ordered mesoporous thin-film templates derived from block copolymer self-assembly, in combination with transient laser heating, enabled molding of crystalline silicon via a liquid phase process at the nanoscale to prepare 3D periodically ordered crystalline silicon (c-Si) mesostructures with orthorhombic space group *F*222. The thin-film templates with 3D continuous network structures were derived from spin-coating block copolymer–additive hybrid solutions and subsequent solvent vapor annealing-based self-assembly. Mesoporous gyroidal templates from pyrolyzed all-organic block copolymer–resols composites survived the high processing temperatures exceeding 1410 °C as a result of ultrashort (nanoseconds) melting durations, leading to excellent pattern transfer fidelity from the block copolymer-directed structure into c-Si. All processing steps utilized in our experiments are compatible with present day semiconductor nanofabrication. We therefore expect that our results are relevant to industrial applications. Furthermore, since a range of other materials including semiconductors and metals are amenable to this type of processing as a result of similar or lower melting temperatures, we expect this work to enable access to a range of advanced thin film materials with interesting electronic, photonic, and phononic properties.[33,58–60] The 3D network structure of templates and final c-Si mesostructures resulted from uniaxial compression of the alternating gyroid morphology during thin film processing. Analysis of structural details of the template and resulting c-Si mesostructures as revealed by grazing incidence small-angle scattering experiments were consistent with reduced *F*222 symmetry. This structure identification has important ramifications for structure–property correlations of the final materials. In recent theoretical work this reduction in symmetry from cubic gyroidal to the associated point group symmetry $D_2$ reflects a symmetry constraint that leads to the formation of self-assembled quantum materials in the form of 3D photonic or phononic materials with topologically protected Weyl points.[32] Following this theoretical study, our work now presents an example that illustrates how to achieve such symmetry constraints in an experimental system, thereby taking a substantial step in the direction of the exciting emerging field of block copolymer self-assembly directed quantum materials.

## METHODS

**Fabrication of Periodically Ordered Mesoporous Thin-Film Network Templates.** The ISO triblock terpolymer (TTP) was synthesized via sequential anionic polymerization, while resorcinol resols, the carbon precursors, were synthesized by condensation reaction between resorcinol and formaldehyde, both as described elsewhere.[19,61] A combination of proton nuclear magnetic resonance ($^1$H NMR) and gel permeation chromatography (GPC) was used to determine the ISO total number-average molar mass ($M_n$) of 77.3 kg/mol and a polydispersity index (PDI) of 1.04, with the volume fractions of PI, PS, and PEO blocks being 30.6%, 60.8%, and 8.6%, respectively. The densities used for calculating volume fractions of PI, PS, and PEO blocks were 0.830 g/cm$^3$, 0.969 g/cm$^3$, and 1.06 g/cm$^3$, respectively.

The procedure to prepare resin/carbon thin-film networks followed what has been reported previously.[26] In short, a 5.0 wt % solution in anhydrous tetrahydrofuran (THF) of ISO and resols (Figure 1a) was


https://dx.doi.org/10.1021/acsnano.0c03150
ACS Nano 2020, 14, 11273–11282

spin-coated on Si wafers with native oxide at 3000 rpm. The combined volume of the PEO block and resols domain accounted for 24% of the ISO–resols hybrid (1.1 g/cm$^3$ was used as the density of resols). The resulting polymeric thin films were subjected to SVA using THF in a home-built apparatus.[26] The films were first swollen by 1.5 standard cubic feet per hour (SCFH) flow of argon through THF (wet argon). The dry argon flow rate was then increased, while the wet argon flow rate was decreased stepwise until a ratio of 0.4 SCFH (wet argon) to 1.0 SCFH (dry argon) was reached. Finally, SVA was concluded by quenching the ordered structures in a copious amount of dry argon (Figure 1b). After cross-linking the resols at 120 °C for 24 h, pyrolysis at 450 or 600 °C for 3 h under nitrogen flow in a tube furnace yielded ordered mesoporous resin/carbon thin films supported on Si wafers (Figure 1c).

**Amorphous Si Deposition.** The mesoporous thin films were first cleaned by immersing them in a bath prepared from deionized (DI) water, 37% to 38% hydrochloric acid (HCl), and 30% hydrogen peroxide ($H_2O_2$) in a volumetric ratio of 6:1:1 (6:1:1, v/v/v), for 10 min at 72 °C. After rinsing with DI water, the films were dipped in 49% hydrofluoric acid (HF) diluted by DI water (1:20, v/v) for 10 min at room temperature (Caution: exercise extreme care when handling HF and follow appropriate standard operating procedures). After rinsing with DI water and dry blowing with nitrogen, the carbon thin films were immediately loaded into a quartz furnace for low pressure chemical vapor deposition (LPCVD) of amorphous silicon (a-Si) from the $SiH_4$ silane precursor. LPCVD took place at 570 °C for 25 min, with the chamber pressure at 150 mTorr and silane flow rate of 150 standard cubic centimeters per minute (SCCM). In addition to entering the mesoporous network pores, a-Si also formed an excess overlayer on the top surface of the films (Figure 1d). During this processing step all films were exposed to almost 600 °C for extended periods of time. As a result, in the main text we refer to these films after the a-Si deposition as carbon rather than resin films.

**Transient Excimer Laser Annealing.** The description of the excimer laser system was detailed previously.[24,31] A 308 nm wavelength, 35 ns fwhm, XeCl excimer laser beam was used to irradiate the thin films at normal incidence after a-Si deposition. A fluence of 630 mJ/cm$^2$, above the single crystal Si melt threshold of 600 mJ/cm$^2$, was used to induce a total melt duration of approximately 50 ns (c-Si, Figure 1e). The area of each laser spot was approximately 3 mm × 3 mm, and the surface reflectance at the center of the irradiated area was recorded using a 650 nm diode laser incident at 40° with respect to the film normal.

**Removal of Template.** After transient laser annealing, the remaining Si overlayer on top of the carbon and c-Si composite thin films was removed by reactive ion etching (RIE) for 45 s with $CF_4$ followed by 5 min with $O_2$ at 150 W employing an Oxford PlasmaLab 80+ etcher. After a 2 min dip in 49% HF to remove silicon oxide generated in the last step, the wafers were cleaved into small pieces to expose the underlying carbon and c-Si networks. To reveal the pure c-Si networks, the carbon template was etched away for 6 to 10 h at 75 °C by piranha solution freshly prepared by adding concentrated sulfuric acid ($H_2SO_4$) to 30% $H_2O_2$ (3:1, v/v) (Caution: exercise extra care when adding $H_2SO_4$ to $H_2O_2$, minimize amount of piranha used, and avoid contact with organic substances).

**Structure Characterization.** Scanning electron microscopy (SEM) images were captured with an in-beam secondary electron detector using a Tescan Mira3 field emission scanning electron microscope (FESEM) operating at a 5 kV accelerating voltage (Figure 2a,b) or with an inlens EsB detector using a Zeiss GeminiSEM 500 operating at a 5 kV (Figure 2c) accelerating voltage.

High-resolution transmission electron microscopy (TEM) images of thin film cross sections (Figure S12) were captured with an FEI Tecnai F20 TEM operating at 200 keV. The sample section was prepared using a Thermo Fisher Helios G4 UX focused-ion beam (FIB) instrument.

Level set calculations were performed using MATLAB with additional coordinate transformations in order to compare experimental SEM-based surface morphologies with expectations from different Miller planes.[48]

2D grazing incidence small-angle X-ray scattering (GISAXS) data were recorded using a Pilatus 200k pixel array detector at the D1 beam station at the Cornell High Energy Synchrotron Source (CHESS, for Figure 3a–c) or using a Pilatus 1 M pixel array detector at the 12-ID Soft Matter Interfaces (SMI) beamline at the National Synchrotron Light Source II (NSLS II, for Figure 3d). The incident X-ray energies were 10.7 keV at CHESS and 16.1 keV at NSLS II, and the sample to detector distances (SDD) were 1.86 m at CHESS and 7.49 m at NSLS II. Incident angles ranged between 0.1° and 0.2° and were chosen in order to maximize signal-to-noise for each sample.

2D GISAXS data were processed and plotted using the MATLAB-based software GIXSGUI (version 1.7.1)[62] to have $q_y$ on the horizontal axis and $q_z$ on the vertical axis. $q_y$ and $q_z$ were the components of the scattering vector, $q = 4\pi \sin \theta/\lambda$, along the directions parallel and perpendicular to the film surface, respectively. $2\theta$ is the scattering angle, and $\lambda$ is the wavelength of the X-rays. The expected peak positions for peak indexing were calculated based on the distorted-wave Born approximation (DWBA).

## ASSOCIATED CONTENT

### Supporting Information

The Supporting Information is available free of charge at https://pubs.acs.org/doi/10.1021/acsnano.0c03150.

SEM and TEM images and GISAXS patterns of thin film structures, simulated thin film structures, and a schematic illustrating the lattice transformations observed in this study (PDF)

## AUTHOR INFORMATION


### Corresponding Author

**Ulrich B. Wiesner** – *Department of Materials Science and Engineering, Cornell University, Ithaca, New York 14853, United States;* orcid.org/0000-0001-6934-3755; Email: ubw1@cornell.edu

### Authors

**Fei Yu** – *Department of Materials Science and Engineering and Department of Chemistry and Chemical Biology, Cornell University, Ithaca, New York 14853, United States;* orcid.org/0000-0002-8191-8096

**Qi Zhang** – *Department of Materials Science and Engineering, Cornell University, Ithaca, New York 14853, United States;* orcid.org/0000-0001-5765-4505

**R. Paxton Thedford** – *Department of Materials Science and Engineering and Robert Frederick Smith School of Chemical and Biomolecular Engineering, Cornell University, Ithaca, New York 14853, United States;* orcid.org/0000-0003-0811-227X

**Andrej Singer** – *Department of Materials Science and Engineering, Cornell University, Ithaca, New York 14853, United States;* orcid.org/0000-0002-2965-9242

**Detlef-M. Smilgies** – *Robert Frederick Smith School of Chemical and Biomolecular Engineering and Cornell High Energy Synchrotron Source, Cornell University, Ithaca, New York 14853, United States;* orcid.org/0000-0001-9351-581X

**Michael O. Thompson** – *Department of Materials Science and Engineering, Cornell University, Ithaca, New York 14853, United States*

Complete contact information is available at: https://pubs.acs.org/10.1021/acsnano.0c03150


### Author Contributions

$^{\perp}$(F.Y. and Q.Z.) Equal contribution.



https://dx.doi.org/10.1021/acsnano.0c03150
ACS Nano 2020, 14, 11273–11282

### Notes

The authors declare no competing financial interest.

## ACKNOWLEDGMENTS

Funding support from the National Science Foundation (NSF DMR-1707836) for this work is gratefully acknowledged. We made use of shared facilities at the Cornell Center for Materials Research, which is supported through the NSF MRSEC program (DMR-1719875), and at the Cornell NanoScale Facility, a member of the National Nanotechnology Coordinated Infrastructure (NNCI), which is supported by the National Science Foundation (NNCI1542081). GISAXS experiments were conducted at the Cornell High Energy Synchrotron Source (CHESS) supported by the National Science Foundation (DMR-1332208) and 12-ID Soft Matter Interfaces (SMI) beamline at National Synchrotron Light Source, a U.S. Department of Energy (DOE) Office of Science User Facility operated for the DOE Office of Science by Brookhaven National Laboratory under Contract No. DE-AC02-98CH10886. R.P.T. was supported by the NSF Graduate Research Fellowship Program under Grant Number DGE-1650441. We thank S. M. Gruner and M. Fruchart for helpful discussions and P. A. Beaucage for experimental setup.

## REFERENCES

(1) Ito, T.; Okazaki, S. Pushing the Limits of Lithography. *Nature* **2000**, *406*, 1027−1031.
(2) Braun, P. V. Materials Chemistry in 3D Templates for Functional Photonics. *Chem. Mater.* **2014**, *26*, 277−286.
(3) Vogel, N.; Retsch, M.; Fustin, C.-A.; del Campo, A.; Jonas, U. Advances in Colloidal Assembly: The Design of Structure and Hierarchy in Two and Three Dimensions. *Chem. Rev.* **2015**, *115*, 6265−6311.
(4) Inoue, T.; Soen, T.; Hashimoto, T.; Kawai, H. Thermodynamic Interpretation of Domain Structure in Solvent-Cast Films of A-B Type Block Copolymers of Styrene and Isoprene. *J. Polym. Sci. Part A-2: Polym. Phys.* **1969**, *7*, 1283−1301.
(5) Hajduk, D. A.; Harper, P. E.; Gruner, S. M.; Honeker, C. C.; Kim, G.; Thomas, E. L.; Fetters, L. J. The Gyroid: A New Equilibrium Morphology in Weakly Segregated Diblock Copolymers. *Macromolecules* **1994**, *27*, 4063−4075.
(6) Epps, T. H.; Cochran, E. W.; Bailey, T. S.; Waletzko, R. S.; Hardy, C. M.; Bates, F. S. Ordered Network Phases in Linear Poly(isoprene-*b*-styrene-*b*-ethylene oxide) Triblock Copolymers. *Macromolecules* **2004**, *37*, 8325−8341.
(7) Warren, S. C.; DiSalvo, F. J.; Wiesner, U. Nanoparticle-Tuned Assembly and Disassembly of Mesostructured Silica Hybrids. *Nat. Mater.* **2007**, *6*, 156−161.
(8) Garcia, B. C.; Kamperman, M.; Ulrich, R.; Jain, A.; Gruner, S. M.; Wiesner, U. Morphology Diagram of a Diblock Copolymer—Aluminosilicate Nanoparticle System. *Chem. Mater.* **2009**, *21*, 5397−5405.
(9) Hur, K.; Wiesner, U. Design and Applications of Multiscale Organic−Inorganic Hybrid Materials Derived from Block Copolymer Self-Assembly. In *Hierarchical Macromolecular Structures: 60 Years after the Staudinger Nobel Prize II*; Percec, V., Ed.; Springer International Publishing: Cham, 2013; pp 259−293.
(10) Hoheisel, T. N.; Hur, K.; Wiesner, U. B. Block Copolymer-Nanoparticle Hybrid Self-Assembly. *Prog. Polym. Sci.* **2015**, *40*, 3−32.
(11) Chan, V. Z.-H.; Hoffman, J.; Lee, V. Y.; Iatrou, H.; Avgeropoulos, A.; Hadjichristidis, N.; Miller, R. D.; Thomas, E. L. Ordered Bicontinuous Nanoporous and Nanorelief Ceramic Films from Self Assembling Polymer Precursors. *Science* **1999**, *286*, 1716−1719.
(12) Simon, P. F. W.; Ulrich, R.; Spiess, H. W.; Wiesner, U. Block Copolymer-Ceramic Hybrid Materials from Organically Modified Ceramic Precursors. *Chem. Mater.* **2001**, *13*, 3464−3486.
(13) Olson, D. A.; Chen, L.; Hillmyer, M. A. Templating Nanoporous Polymers with Ordered Block Copolymers. *Chem. Mater.* **2008**, *20*, 869−890.
(14) Lee, J.; Orilall, M. C.; Warren, S. C.; Kamperman, M.; DiSalvo, F. J.; Wiesner, U. Direct Access to Thermally Stable and Highly Crystalline Mesoporous Transition-Metal Oxides with Uniform Pores. *Nat. Mater.* **2008**, *7*, 222−228.
(15) Tavakkoli K. G., A.; Gotrik, K. W.; Hannon, A. F.; Alexander-Katz, A.; Ross, C. A.; Berggren, K. K. Templating Three-Dimensional Self-Assembled Structures in Bilayer Block Copolymer Films. *Science* **2012**, *336*, 1294−1298.
(16) Majewski, P. W.; Rahman, A.; Black, C. T.; Yager, K. G. Arbitrary Lattice Symmetries *via* Block Copolymer Nanomeshes. *Nat. Commun.* **2015**, *6*, 7448.
(17) Liu, G.; Detcheverry, F.; Ramírez-Hernández, A.; Yoshida, H.; Tada, Y.; de Pablo, J. J.; Nealey, P. F. Nonbulk Complex Structures in Thin Films of Symmetric Block Copolymers on Chemically Nanopatterned Surfaces. *Macromolecules* **2012**, *45*, 3986−3992.
(18) Meng, Y.; Gu, D.; Zhang, F.; Shi, Y.; Cheng, L.; Feng, D.; Wu, Z.; Chen, Z.; Wan, Y.; Stein, A.; Zhao, D. A Family of Highly Ordered Mesoporous Polymer Resin and Carbon Structures from Organic−Organic Self-Assembly. *Chem. Mater.* **2006**, *18*, 4447−4464.
(19) Werner, J. G.; Hoheisel, T. N.; Wiesner, U. Synthesis and Characterization of Gyroidal Mesoporous Carbons and Carbon Monoliths with Tunable Ultralarge Pore Size. *ACS Nano* **2014**, *8*, 731−743.
(20) Werner, J. G.; Rodríguez-Calero, G. G.; Abruña, H. D.; Wiesner, U. Block Copolymer Derived 3-D Interpenetrating Multifunctional Gyroidal Nanohybrids for Electrical Energy Storage. *Energy Environ. Sci.* **2018**, *11*, 1261−1270.
(21) Ryoo, R.; Joo, S. H.; Jun, S. Synthesis of Highly Ordered Carbon Molecular Sieves *via* Template-Mediated Structural Transformation. *J. Phys. Chem. B* **1999**, *103*, 7743−7746.
(22) Werner, J. G.; Scherer, M. R. J.; Steiner, U.; Wiesner, U. Gyroidal Mesoporous Multifunctional Nanocomposites *via* Atomic Layer Deposition. *Nanoscale* **2014**, *6*, 8736−8742.
(23) Cowman, C. D.; Padgett, E.; Tan, K. W.; Hovden, R.; Gu, Y.; Andrejevic, N.; Muller, D.; Coates, G. W.; Wiesner, U. Multicomponent Nanomaterials with Complex Networked Architectures from Orthogonal Degradation and Binary Metal Backfilling in ABC Triblock Terpolymers. *J. Am. Chem. Soc.* **2015**, *137*, 6026−6033.
(24) Tan, K. W.; Jung, B.; Werner, J. G.; Rhoades, E. R.; Thompson, M. O.; Wiesner, U. Transient Laser Heating Induced Hierarchical Porous Structures from Block Copolymer-Directed Self-Assembly. *Science* **2015**, *349*, 54−58.
(25) Tan, K. W.; Werner, J. G.; Goodman, M. D.; Kim, H. S.; Jung, B.; Sai, H.; Braun, P. V.; Thompson, M. O.; Wiesner, U. Synthesis and Formation Mechanism of All-Organic Block Copolymer-Directed Templating of Laser-Induced Crystalline Silicon Nanostructures. *ACS Appl. Mater. Interfaces* **2018**, *10*, 42777−42785.
(26) Zhang, Q.; Matsuoka, F.; Suh, H. S.; Beaucage, P. A.; Xiong, S.; Smilgies, D.-M.; Tan, K. W.; Werner, J. G.; Nealey, P. F.; Wiesner, U. B. Pathways to Mesoporous Resin/Carbon Thin Films with Alternating Gyroid Morphology. *ACS Nano* **2018**, *12*, 347−358.
(27) Yin, Y.; Rioux, R. M.; Erdonmez, C. K.; Hughes, S.; Somorjai, G. A.; Alivisatos, A. P. Formation of Hollow Nanocrystals through the Nanoscale Kirkendall Effect. *Science* **2004**, *304*, 711−714.
(28) Chen, Q.; Sieradzki, K. Spontaneous Evolution of Bicontinuous Nanostructures in Dealloyed Li-Based Systems. *Nat. Mater.* **2013**, *12*, 1102−1106.
(29) Jung, B.; Sha, J.; Paredes, F.; Chandhok, M.; Younkin, T. R.; Wiesner, U.; Ober, C. K.; Thompson, M. O. Kinetic Rates of Thermal Transformations and Diffusion in Polymer Systems Measured during Submillisecond Laser-Induced Heating. *ACS Nano* **2012**, *6*, 5830−5836.


https://dx.doi.org/10.1021/acsnano.0c03150
*ACS Nano* 2020, 14, 11273−11282

(30) Tan, K. W.; Wiesner, U. Block Copolymer Self-Assembly Directed Hierarchically Structured Materials from Nonequilibrium Transient Laser Heating. *Macromolecules* **2019**, *52*, 395−409.
(31) Arora, H.; Du, P.; Tan, K. W.; Hyun, J. K.; Grazul, J.; Xin, H. L.; Muller, D. A.; Thompson, M. O.; Wiesner, U. Block Copolymer Self-Assembly−Directed Single-Crystal Homo- and Heteroepitaxial Nanostructures. *Science* **2010**, *330*, 214−219.
(32) Fruchart, M.; Jeon, S.-Y.; Hur, K.; Cheianov, V.; Wiesner, U.; Vitelli, V. Soft Self-Assembly of Weyl Materials for Light and Sound. *Proc. Natl. Acad. Sci. U. S. A.* **2018**, *115*, E3655−E3664.
(33) Robbins, S. W.; Beaucage, P. A.; Sai, H.; Tan, K. W.; Werner, J. G.; Sethna, J. P.; DiSalvo, F. J.; Gruner, S. M.; Van Dover, R. B.; Wiesner, U. Block Copolymer Self-Assembly−Directed Synthesis of Mesoporous Gyroidal Superconductors. *Sci. Adv.* **2016**, *2*, No. e1501119.
(34) Chatterjee, J.; Jain, S.; Bates, F. S. Comprehensive Phase Behavior of Poly(isoprene-*b*-styrene-*b*-ethylene oxide) Triblock Copolymers. *Macromolecules* **2007**, *40*, 2882−2896.
(35) Khandpur, A. K.; Foerster, S.; Bates, F. S.; Hamley, I. W.; Ryan, A. J.; Bras, W.; Almdal, K.; Mortensen, K. Polyisoprene-Polystyrene Diblock Copolymer Phase Diagram near the Order-Disorder Transition. *Macromolecules* **1995**, *28*, 8796−8806.
(36) Floudas, G.; Vazaiou, B.; Schipper, F.; Ulrich, R.; Wiesner, U.; Iatrou, H.; Hadjichristidis, N. Poly(ethylene oxide-*b*-isoprene) Diblock Copolymer Phase Diagram. *Macromolecules* **2001**, *34*, 2947−2957.
(37) Robbins, S. W.; Sai, H.; DiSalvo, F. J.; Gruner, S. M.; Wiesner, U. Monolithic Gyroidal Mesoporous Mixed Titanium-Niobium Nitrides. *ACS Nano* **2014**, *8*, 8217−8223.
(38) Weller, T.; Deilmann, L.; Timm, J.; Dörr, T. S.; Beaucage, P. A.; Cherevan, A. S.; Wiesner, U. B.; Eder, D.; Marschall, R. A Crystalline and 3D Periodically Ordered Mesoporous Quaternary Semiconductor for Photocatalytic Hydrogen Generation. *Nanoscale* **2018**, *10*, 3225−3234.
(39) Warren, S. C.; Messina, L. C.; Slaughter, L. S.; Kamperman, M.; Zhou, Q.; Gruner, S. M.; DiSalvo, F. J.; Wiesner, U. Ordered Mesoporous Materials from Metal Nanoparticle-Block Copolymer Self-Assembly. *Science* **2008**, *320*, 1748−1752.
(40) Kamperman, M.; Du, P.; Scarlat, R. O.; Herz, E.; Werner-Zwanziger, U.; Graf, R.; Zwanziger, J. W.; Spiess, H. W.; Wiesner, U. Composition and Morphology Control in Ordered Mesostructured High-Temperature Ceramics from Block Copolymer Mesophases. *Macromol. Chem. Phys.* **2007**, *208*, 2096−2108.
(41) Lunkenbein, T.; Rosenthal, D.; Otremba, T.; Girgsdies, F.; Li, Z.; Sai, H.; Bojer, C.; Auffermann, G.; Wiesner, U.; Breu, J. Access to Ordered Porous Molybdenum Oxycarbide/Carbon Nanocomposites. *Angew. Chem., Int. Ed.* **2012**, *51*, 12892−12896.
(42) Haske, W.; Chen, V. W.; Hales, J. M.; Dong, W.; Barlow, S.; Marder, S. R.; Perry, J. W. 65 nm Feature Sizes Using Visible Wavelength 3-D Multiphoton Lithography. *Opt. Express* **2007**, *15*, 3426−3436.
(43) Crossland, E. J. W.; Kamperman, M.; Nedelcu, M.; Ducati, C.; Wiesner, U.; Smilgies, D.-M.; Toombes, G. E. S.; Hillmyer, M. A.; Ludwigs, S.; Steiner, U.; Snaith, H. J. A Bicontinuous Double Gyroid Hybrid Solar Cell. *Nano Lett.* **2009**, *9*, 2807−2812.
(44) Kern, W. The Evolution of Silicon Wafer Cleaning Technology. *J. Electrochem. Soc.* **1990**, *137*, 1887−1892.
(45) Urech, L.; Lippert, T. Photoablation of Polymer Materials. In *Photochemistry and Photophysics of Polymer Materials*; Allen, N. S., Ed.; John Wiley & Sons: Hoboken, 2010; pp 541−568.
(46) Grove, A. S. *Physics and Technology of Semiconductor Devices*; John Wiley & Sons: Hoboken, 1967; p 30.
(47) Aroyo, M. I., Ed. *International Tables for Crystallography Vol. A: Space-group symmetry*; John Wiley & Sons: Hoboken, 2016; pp 193−687.
(48) Wohlgemuth, M.; Yufa, N.; Hoffman, J.; Thomas, E. L. Triply Periodic Bicontinuous Cubic Microdomain Morphologies by Symmetries. *Macromolecules* **2001**, *34*, 6083−6089.
(49) Falcaro, P.; Grosso, D.; Amenitsch, H.; Innocenzi, P. Silica Orthorhombic Mesostructured Films with Low Refractive Index and High Thermal Stability. *J. Phys. Chem. B* **2004**, *108*, 10942−10948.
(50) Stefik, M.; Wang, S.; Hovden, R.; Sai, H.; Tate, M. W.; Muller, D. A.; Steiner, U.; Gruner, S. M.; Wiesner, U. Networked and Chiral Nanocomposites from ABC Triblock Terpolymer Coassembly with Transition Metal Oxide Nanoparticles. *J. Mater. Chem.* **2012**, *22*, 1078−1087.
(51) Li, Z.; Hur, K.; Sai, H.; Higuchi, T.; Takahara, A.; Jinnai, H.; Gruner, S. M.; Wiesner, U. Linking Experiment and Theory for Three-Dimensional Networked Binary Metal Nanoparticle-Triblock Terpolymer Superstructures. *Nat. Commun.* **2014**, *5*, 3247.
(52) Feng, X.; Burke, C. J.; Zhuo, M.; Guo, H.; Yang, K.; Reddy, A.; Prasad, I.; Ho, R.-M.; Avgeropoulos, A.; Grason, G. M.; Thomas, E. L. Seeing Mesoatomic Distortions in Soft-Matter Crystals of a Double-Gyroid Block Copolymer. *Nature* **2019**, *575*, 175−179.
(53) Yoneda, Y. Anomalous Surface Reflection of X Rays. *Phys. Rev.* **1963**, *131*, 2010−2013.
(54) Hatalis, M. K.; Greve, D. W. Large Grain Polycrystalline Silicon by Low Temperature Annealing of Low-Pressure Chemical Vapor Deposited Amorphous Silicon Films. *J. Appl. Phys.* **1988**, *63*, 2260−2266.
(55) Thompson, M. O.; Galvin, G. J.; Mayer, J. W.; Peercy, P. S.; Poate, J. M.; Jacobson, D. C.; Cullis, A. G.; Chew, N. G. Melting Temperature and Explosive Crystallization of Amorphous Silicon during Pulsed Laser Irradiation. *Phys. Rev. Lett.* **1984**, *52*, 2360−2363.
(56) Auston, D. H.; Surko, C. M.; Venkatesan, T. N. C.; Slusher, R. E.; Golovchenko, J. A. Time-Resolved Reflectivity of Ion-Implanted Silicon during Laser Annealing. *Appl. Phys. Lett.* **1978**, *33*, 437−440.
(57) Leamy, H. J.; Brown, W. L.; Celler, G. K.; Foti, G.; Gilmer, G. H.; Fan, J. C. C. Explosive Crystallization of Amorphous Germanium. *Appl. Phys. Lett.* **1981**, *38*, 137−139.
(58) Hur, K.; Francescato, Y.; Giannini, V.; Maier, S. A.; Hennig, R. G.; Wiesner, U. Three-Dimensionally Isotropic Negative Refractive Index Materials from Block Copolymer Self-Assembled Chiral Gyroid Networks. *Angew. Chem., Int. Ed.* **2011**, *50*, 11985−11989.
(59) Hur, K.; Hennig, R. G.; Wiesner, U. Exploring Periodic Bicontinuous Cubic Network Structures with Complete Phononic Bandgaps. *J. Phys. Chem. C* **2017**, *121*, 22347−22352.
(60) Bolmatov, D.; Zhang, Q.; Soloviov, D.; Li, Y. M.; Werner, J. G.; Suvorov, A.; Cai, Y. Q.; Wiesner, U.; Zhernenkov, M.; Katsaras, J. Nanoscale *Q*-Resolved Phonon Dynamics in Block Copolymers. *ACS Appl. Nano Mater.* **2018**, *1*, 4918−4926.
(61) Bailey, T. S.; Pham, H. D.; Bates, F. S. Morphological Behavior Bridging the Symmetric AB and ABC States in the Poly(styrene-*b*-isoprene-*b*-ethylene oxide) Triblock Copolymer System. *Macromolecules* **2001**, *34*, 6994−7008.
(62) Jiang, Z. GIXSGUI: A MATLAB Toolbox for Grazing-Incidence X-Ray Scattering Data Visualization and Reduction, and Indexing of Buried Three-Dimensional Periodic Nanostructured Films. *J. Appl. Crystallogr.* **2015**, *48*, 917−926.


https://dx.doi.org/10.1021/acsnano.0c03150
*ACS Nano* 2020, 14, 11273−11282